Convective flow generated by lateral heating on a vertically stable solute gradient

Yu-Hsiang Huang,[1] Falin Chen ,[1] and Chih-Ang Chung[2],*

[1]*Institute of Applied Mechanics, National Taiwan University, Taipei 10674, Taiwan*
[2]*Department of Mechanical Engineering, National Central University, Jhongli 320317, Taiwan*

We conduct a series of three-dimensional computations to investigate the convective flow generated by the interaction between the vertical solute gradient and the horizontal thermal gradient. The first set of computations is carried out under a wide range of boundary values considered by previous experimental studies, which mostly have a strongly stratified solute gradient. Results show that the convection invariably develops into the so-called fully developed flow composed of the largest number of horizontal convection layers under all the conditions considered. Within each layer, there prevails an array of salt-finger vortices. The multilayered structure changes with boundary values systematically, while the convection layer bears a layer thickness so that the positive thermal buoyancy can balance with the negative solute buoyancy. In the second set of computations, we consider the boundary conditions so that the thermal buoyancy is much larger than the solute buoyancy. In such a weakly stratified solute gradient and a thermal-diffusion-dominated environment, the computational domain is filled with a sizeable convective circulation while no salt finger occurs.

I. INTRODUCTION

When a horizontal thermal gradient is applied on a bulk fluid stably stratified by a vertical solute gradient, a series of horizontal convection layers form on the hot wall and develop towards the cold wall when the thermal gradient exceeds the critical condition. The solute-rich and warm fluid moves above the solute-poor and cold fluid within the convection layer, being conducive to a salt-finger convection consisting of a series of vortices with axes pointing from the hot wall to the cold wall. The salt-finger vortices are generated virtually simultaneously with the formation of the convection layers. Both flows develop into a flow containing a large number of convection layers of almost uniform thickness. This flow is the so-called the fully developed salt-finger convective flow and we shall abbreviate it as the fully developed flow afterwards. The fully developed flow persists for a while before the convection layers start to merge when the salinity distribution disperses into relatively uniform. For details of the flow evolution, the reader is referred to, for example, Refs. [1–5], among others.

In the early stage of research, most attention was paid to the formation of the convection layer and the layer thickness measurement, which was supposed to be the characteristic length of the convective flow. Chen *et al.* [2] proposed an empirical formula for the layer thickness,

$$h_T = \frac{\alpha \Delta T}{-\beta dS/dz},$$ (1)

*Corresponding author: cachung@ncu.edu.tw

in which α and β are volumetric expansion coefficients due to heat and solute, respectively, ΔT is the horizontal temperature difference applied, and dS/dz is the vertical solute gradient. After measuring the layer thickness from a series of experiments having a vertical solute gradient subjected to impulsive lateral heating of different scales, they concluded that the layer thickness decreases from $0.97h_T$ to $0.67h_T$ when the thermal Rayleigh number $\mathrm{Ra} = g\alpha\Delta Th^3/\nu\kappa_T$ increases from 1.4×10^4 to 5.4×10^4, where g is the gravitational constant, h is the layer thickness measured from experiments, ν is the kinematic viscosity, and κ_T is the thermal diffusivity. This conclusion was supported by the experiments of Huppert and Turner [3] and Huppert $et\ al.$ [6] that the layer thickness decreases asymptotically to $0.6h_T$ when Ra increases from 10^6 to 10^9. In these experiments, the layer thickness was measured when the convective flow became fully developed. Since that moment the flow consisted of the largest number of convection layers of virtually uniform thickness, which was supposed to be the representative structure predominating the unsteady flow.

In addition to the layer thickness, the convection layer stability was another issue having been explored. Kerr [7] conducted a stability analysis for the interleaving intrusion layer. He extended the stability analysis by considering the salt finger and concluded that the salt finger is more unstable than the interleaving layer while the two flows have a similar growth rate [8]. This conclusion was confirmed by Chan $et\ al.$ [5], who examined the transverse mode stabilities corresponding to the convection layer and the longitudinal mode corresponding to the salt finger, that the longitudinal mode is slightly more unstable than the transverse mode. They also illustrated that, for both the transverse and longitudinal modes, the flow could be categorized into three different flow regimes: thermal diffusion, salt finger, and solute diffusion. However, their stability analyses were implemented in the two-dimensional domain, which was extended to three dimensional by Chang $et\ al.$ [9]. They concluded that the longitudinal mode is generally more unstable than the transverse mode. Namely, the salt-finger flow is invariably less stable than the convection layer, while the stability criteria of these two flows bear only a small difference. This conclusion explains why, in most experimental studies, the formation of the convection layer and the salt finger occurred virtually simultaneously.

Previous experimental studies showed consistently that the present convective flow is highly nonlinear and unsteady. The linear stability analysis, however, can only examine the convective flow at the onset. Nonlinear computation, accordingly, shall be pursued to gain the details of the flow evolution. In doing so, Wirt and Liu [10] and Heinrich [11] carried out a series of finite-difference computations for the narrow slot flow investigated in Thorpe $et\ al.$ [1], while Lee and Hyun [12] performed the computations in a wide-rectangular container. Kamakura and Ozoe [13] computed the same flow while paying particular attention to the merging of adjacent convection layers. Unfortunately, all these nonlinear computations were implemented in the two-dimensional domain; namely, only the convection layer was studied while the salt finger was ignored.

The literature survey above illustrates, in general, that the experimental studies focused on the fully developed flow, the stability analyses emphasized the competition between convection modes at the onset, and the nonlinear computations examined the flow in the two-dimensional domain. These results can hardly integrate into a complete picture of the change of the flow in the entire development process, which can be obtained by pursuing an investigation into the unsteady flow in the three-dimensional domain. Accordingly, in the present study, we conduct a series of nonlinear computations in the three-dimensional domain to simulate the simultaneous occurrence of the convection layer and the salt finger. Close attention will be paid to the unsteadiness of both flows to investigate the physical insights. In the following, we first specify the mathematical formulation and computational procedure in Sec. II. We then simulate an experimental case to examine the three-dimensional flow structure and ensure the correctness of the computation in Sec. III. We show in Sec. IV that the unsteady flow will invariably approach the fully developed flow and illustrate its characteristics from different perspectives. To explore the flow unsteadiness, we investigate in Sec. V the flow transition from the beginning to fully developed. In Sec. VI, we turn to examine the flow in the thermal-diffusion regime in which neither the fully developed flow nor the salt finger occurs. Finally, we summarize a conclusion in Sec. VII.
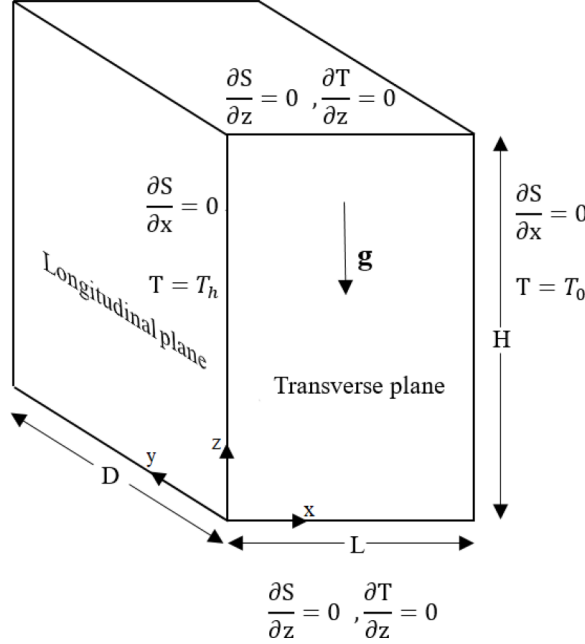
FIG. 1. The computational domain and boundary conditions considered.

II. MATHEMATICAL FORMULATION AND COMPUTATIONAL PROCECEDURE

Consider a rectangular box of a height H, a width L, and a depth D, and the origin of the Cartesian coordinate locates on the front-left corner of the box, as shown in Fig. 1. The box is enclosed with six flat walls on which the no-slip condition applies. The temperatures at the two vertical side walls fix respectively at T_h and T_0 while the heat insulation is prescribed at the other walls. Regarding the solute boundary condition, no solute flux is allowed to conduct through the six walls. Within the box, the fluid stratifies stably with a vertical solute gradient, having a low concentration S_0 at the top ($z = H$) and a high concentration S_h at the bottom ($z = 0$). The initial temperature of the solution is uniformly T_0 in the whole box. At the beginning of the computation, a temperature T_h higher than T_0 is applied impulsively at the left wall ($x = 0$) while the temperature at the right wall ($x = L$) remains at T_0.

To compute the convective flow within the box, the continuity equation, the Navier-Stokes equations, the heat transfer equation, and the solute transfer equation are simultaneously applied. They are, respectively,

$$\nabla \cdot \mathbf{u} = 0, \tag{2}$$

$$\frac{\partial \mathbf{u}}{\partial t} + \mathbf{u} \cdot \nabla \mathbf{u} = -\nabla p + \mathrm{Pr}\nabla^2 \mathbf{u} + \mathrm{Pr}(\mathrm{Ra}_T T - \mathrm{Ra}_S S)\mathbf{k}, \tag{3}$$

$$\frac{\partial T}{\partial t} + \mathbf{u} \cdot \nabla T = \nabla^2 T, \tag{4}$$

$$\frac{\partial S}{\partial t} + \mathbf{u} \cdot \nabla S = \frac{1}{\mathrm{Le}}\nabla^2 S. \tag{5}$$

In the above equations, $\mathbf{u} = (u, v, w)$ is the velocity, $\mathbf{k}$ is the unit vector at the z direction, and the Boussinesq approximation is considered to govern the buoyancy effect. After nondimensionalizing
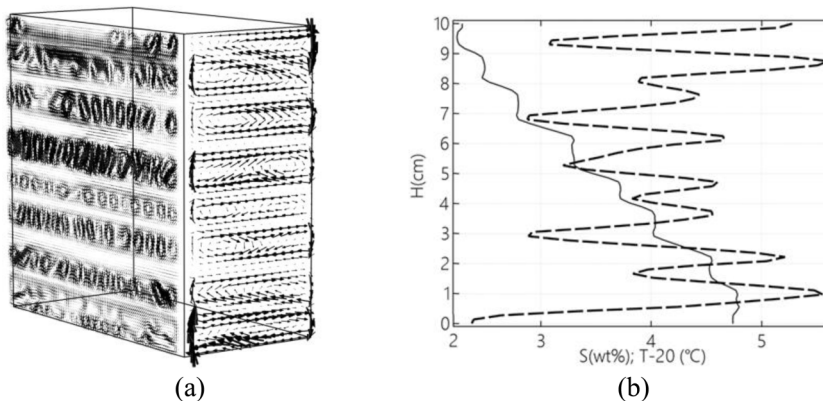
FIG. 2. The computational results simulating experiment 8 of Chen and Chen [4]. (a) The convection cells on the transverse plane at $y = D/2$ and the longitudinal plane at $x = L/2$. (b) The computational results of the solute (solid curve) and temperature (dashed curve) distributions at $t = 39$ min.

the equations with relevant characteristic scales, we end up with four physical parameters,

$$\mathrm{Ra}_T = \frac{g\alpha\Delta T H^3}{\nu\kappa_T}, \quad \mathrm{Ra}_S = \frac{g\beta\Delta S H^3}{\nu\kappa_\mathrm{T}}, \quad \mathrm{Pr} = \frac{\nu}{\kappa_T}, \quad \mathrm{Le} = \frac{\kappa_T}{\kappa_S}, \tag{6}$$

which are respectively the thermal Rayleigh number, the solute Rayleigh number, the Prandtl number, and the Lewis number. In these parameters, **g** is the gravity constant, H is the height of the box, $\Delta T = T_h - T_0$ is the horizontal temperature difference between the two vertical walls, ν is the kinematic viscosity, κ_T is the thermal diffusivity, $\Delta S = S_h - S_0$ is the solute difference between the bottom and the top, and κ_S is the solute diffusivity. For the details of the derivation of these equations, the reader may refer to Huang [14] or references therein. Regarding the boundary conditions, as shown in Fig. 1, the nonslip condition is prescribed on the walls of the box, and the constant temperature $T = T_h$ on the left wall and $T = T_0$ on the right wall. No salinity flux is allowed on all the walls, while heat insulation is applied on all the walls except the left and right vertical walls.

We apply the finite-volume-based solver COMSOL Multiphysics to solve (2)–(5). We need first to use the segregated solver to convert the nonlinear partial differential equations into the linear ones, which are to be solved on each of the grid points. The algebraic multigrid solver is then applied to solve (2) and (3) for the velocity and pressure. The direct solver is used to solve (4) for the temperature and (5) for the salinity. The results will be used as the initial condition for the computation of the next time step. The computational procedure consists of four steps: (a) specify the physical domain and relevant assumptions, (b) prescribe the initial and boundary conditions, (c) discretize the differential equations and build up the computational grid, (d) solve the matrix equations and postprocess the numerical results. We used a desktop PC embedded with a 12-core AMD Ryzen 2920X CPU and 32GB RAM. In general, to finish computing a case, one needs about 60 h of CPU time to get a result like Fig. 2(a) where the unsteady flow has evolved for 2400 s (or 2400 s afterward).

Before the computation begins, the fluid within the box is of a uniform temperature T_0 and a linear solute distribution $S = S_h - \Delta S(z/H)$. When the computation begins, a temperature difference ΔT is applied, together with relevant boundary conditions indicated in Fig. 1. The computations are carried out in a rectangular box of $H = D = 10$ cm and $L = 5$ cm unless otherwise stated. To obtain numerical results with acceptable accuracy and to finish the computation in reasonable computational time, we made several test runs with different computational grids under various time intervals. As a result, we chose a structured hexahedron grid with 50 elements (along the width L)

TABLE I. The physical parameters considered by the experiments of Chen and Chen [4] and the present computation. Please note that for the computations, the unit of S is converted to mol/m^3 and that of β is m^3/mol, which is because of the need for dimensional computations pursued by the present study.

Parameters	Experiments/computations
D (cm)	10
L (cm)	5
H (cm)	10
$\Delta T(^\circ$C)	10
$S_0 \sim S_h$	2–5 wt %(345–885 mol/m^3)
$\rho_0 \sim \rho_h$ (g/cm^3)	1.014–1.036
ν (m^2/s)	1.0035×10^{-6}
α ($^\circ$C^{-1})	3×10^{-4}
β	7.2×10^{-3} wt %$^{-1}$ (4×10^{-5} m^3/mol)
κ_T (m^2/s)	1.42×10^{-7}
κ_S (m^2/s)	1.56×10^{-9}
Pr	7
Le	91

$\times 100$ elements (height H) $\times 100$ elements (depth D) and a time interval of 0.01 s to get a numerical result of adequate accuracy.

III. SIMULATION OF AN EXPERIMENTAL CASE

We begin the investigation with the computation simulating the flow observed by experiment 8 of Chen and Chen [4] in which $\Delta T = 10\,^\circ$C and $\Delta S = 3\%$ corresponding to Ra$_T = 2.11 \times 10^8$ and Ra$_S = 1.52 \times 10^9$, respectively. Relevant parameters considered by both experiment and computation are given in Table I. The purpose of this computation is twofold: to ensure the accuracy of computation and to examine the three-dimensional flow structure.

At the beginning of the computation, the fluid in the box has a uniform temperature of 20 $^\circ$C and a temperature difference $\Delta T = 10\,^\circ$C is impulsively applied on the left wall. Almost immediately, a series of horizontal convection layers form simultaneously along the hot wall, and virtually at the same time, an array of salt-finger vortices is generated in the convection layer to enhance the vertical mixing. At $t = 39$ min, i.e., 39 min into the computation, the flow structure of Fig. 2 demonstrates the velocity vectors taken on the longitudinal plane at $x = L/2$ and the transverse plane at $y = D/2$. After examining the flow structures evolving with time, we found that the flow has reached a status having the most significant number of convection layers. This flow was recognized as the fully developed flow [2,4,5].

For such a fully developed flow as shown in Fig. 2(a), there are eight convection layers on the transverse plane, which is the same as in Fig. 2 of Chen and Chen [4]. In most of the convection layers, an array of salt-finger vortices prevails rigorously. The salt-finger vortices bear a wavelength-to-thickness ratio $\lambda/h_C \approx 0.8$, which are of a similar shape to those shown in Fig. 3 of Chan *et al.* [5] although they considered $\Delta T = 6\,^\circ$C. However, in the top-most and the bottom-most layers, the solute distribution is virtually uniform with a stable temperature gradient, implying that the salt finger can hardly form.

The temperature distribution of Fig. 2(b) appears to be an S shape within each layer, which is approximately symmetric to its horizontal centerline. Simultaneously, the solute distribution is relatively uniform due to the mixing enforced by the salt finger. A region with a large solute gradient
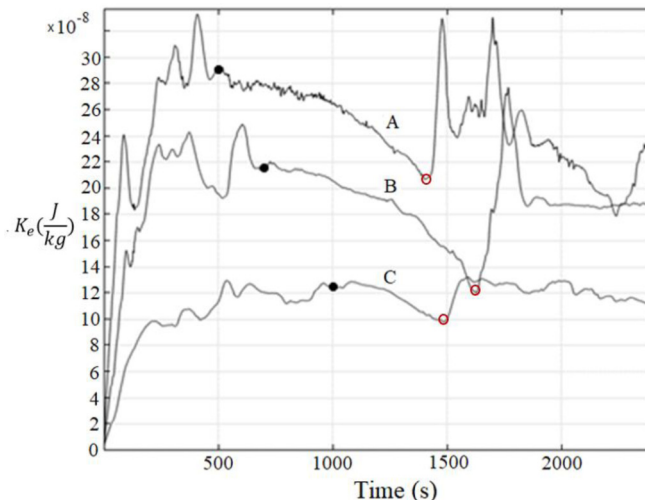
FIG. 3. The time evolutions of the kinetic energy per unit mass averaged over the longitudinal plane at $x = L/2$ for different temperature differences. Curve A corresponds to $\Delta T = 27\,°C$, curve B to $\Delta T = 18\,°C$, curve C to $\Delta T = 11\,°C$. The solid circles stand for the beginning of the fully developed flow and the open circles for the ending of the flow.

at the interface between layers forms a steplike solute structure in the entire height, showing a steplike vertical density structure in double-diffusive interleaving [7]. In comparison with Fig. 2(a) of Chen and Chen [4], it finds that the solute distribution from computation is strikingly similar to the experimental measurement. The overall solute gradient is negative, roughly reflecting the original experimental values 5% at the bottom and 2% at the top, being equivalent to a solute gradient of $-0.3\%\,cm^{-1}$ for a height of 10 cm. The mean temperature within the layer is about $4\,°C$ higher than the initial value $20\,°C$, which is because the hot fluid rises along the heated wall and collectively cumulates the heat within each layer.

IV. FULLY DEVELOPED FLOW

The fully developed flow comprises multiple convection layers filled with salt-finger vortices, as shown in Fig. 2(a). As we will illustrate, the fully developed flow has three features worth elucidating in depth. They are (i) the timing of the fully developed flow, (ii) the layer thickness under different boundary conditions, and (iii) the control of buoyancy balance on the layer thickness. We examine these features by computing the flows generated under a wide range of boundary conditions, and the results are depicted in the following.

A. Timing of the fully developed flow

The first feature to examine is the timing of the fully developed flow, specifically the beginning and the end of the flow. In doing so, we explore the unsteadiness of the flow for the case $\Delta T = 18\,°C$ and $\Delta S = 540\,mol/m^3$ corresponding to $Ra_T = 3.80 \times 10^8$ and $Ra_S = 1.52 \times 10^9$, respectively, and investigate the time evolution of the averaged kinetic energy over the longitudinal plane at $x = L/2$. The result is shown by curve B in Fig. 3. In computing the averaged kinetic energy of a plane, we consider

$$K_e = \frac{\sum_{i=1}^{N} \left(u_i^2 + v_i^2 + w_i^2\right)/2}{N} \tag{7}$$
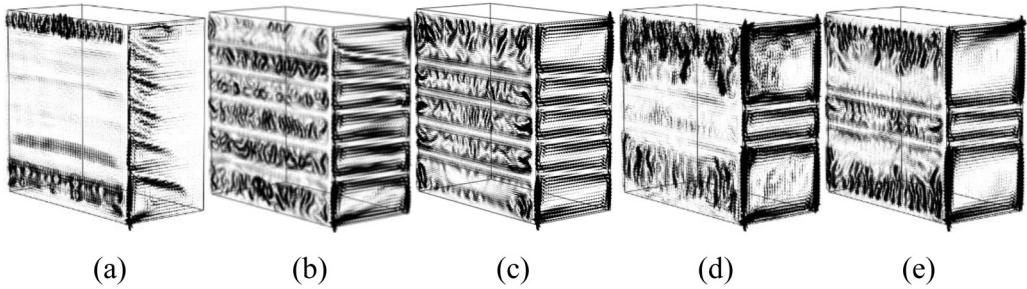
(a)   (b)   (c)   (d)   (e)

FIG. 4. The velocity vectors in the transverse plane at $y = D/2$ and the longitudinal plane at $x = L/2$ for the case $\Delta T = 18\,°C$. The subfigures show the flow at different times: $t =$ (a) 100 s, (b) 375 s, (c) 700 s, (d) 1770 s, (e) 2300 s.

in which K_e is the averaged kinetic energy per unit mass, N is the number of fluid particles (or the grid points), and u, v, w are velocities in, respectively, the x, y, z directions. Since a fluid particle corresponds to a computation grid point, there are $N = 100 \times 100 = 10^4$ particles on a longitudinal plane. On the other hand, we illustrate in Fig. 4 the velocity vectors on both the transverse plane at $y = D/2$ and the longitudinal plane at $x = L/2$ at different times. In the following, we shall examine these two figures simultaneously to look into the unsteadiness of the flow.

At the beginning of the computation, the fluid having a uniform temperature of $20\,°C$ is applied impulsively with a temperature difference $\Delta T = 18\,°C$ on the left wall. Almost immediately, the hot and solute-rich fluid starts to rise along the heated wall quickly [Fig. 4(a)] and the K_e increases rapidly with time as well (curve B of Fig. 3). As soon as the heated fluid rises to a certain height, it turns horizontally to advance into the bulk fluid with an inclined angle towards the bottom. The tilted convection layer reflects the fact that when the fluid moves from the hot wall to the cold wall, it becomes colder faster than it becomes solute poorer due to $\kappa_T \gg \kappa_S$. Consequently, the fluid becomes denser and sinks gradually on the way towards the cold wall. Similar phenomena had been reported by, for example, Chen and Chen (Figs. 1 and 2) [4]. In the present study, the wall temperature increases impulsively by a fixed amount at the beginning of computation. There might occur some interleaving instabilities from the heated wall according to the finite heating rates at the wall, for example, the experiments of Tanny and Tsinober [15] and the discussion of Kerr [16]. This issue may merit another study to investigate the details.

At $t = 375\,s$, the K_e reaches a maximum where the flow is composed of six evenly spaced convection layers. Within each layer, an array of salt fingers lines up, serving to exchange heat and solute between the top and the bottom of the layer; see Fig. 4(b). After passing over the maximum, the K_e first decreases rapidly because of the viscous dissipation resulting from the shear at the interface. It then reaches another maximum at about $t = 600\,s$, which is because, as shown in Fig. 4(c) at $t = 700\,s$, the two convection layers at the top merge into a single layer. The resultant multilayer flow sustains stably for a long time. Accordingly, it was widely recognized as a fully developed flow and was also considered a representative flow by previous experimental studies [2,4,5].

After that, due to the viscous dissipation, the K_e of the fully developed flow decreases gradually while the five-layer structure remains until it runs into another dramatic increase at $t \approx 1610\,s$, as indicated by the open circle. It stands for the end of the fully developed flow because of the dramatic increase of K_e resulting from another merge of the convection layers at both top and bottom boundaries. The layer merge happening at the boundary is an inevitable outcome because the no-solute-flux condition prescribed at both boundaries decreases the solute gradient dS/dz. According to (1), a decrease of dS/dz leads to an increase of h_T, which is materialized through the merging of two layers.
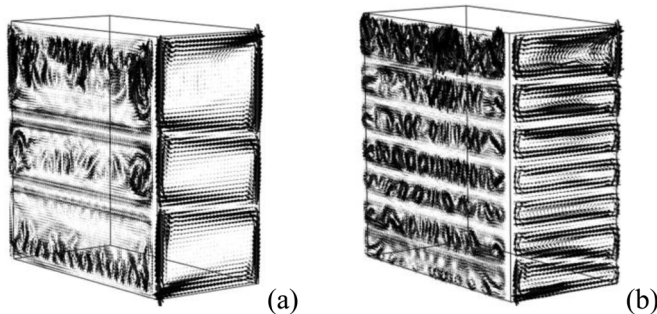
FIG. 5. The velocity vectors in the transverse plane at $y = D/2$ and the longitudinal plane at $x = L/2$ of the fully developed salt-finger convection flows under different ΔT while the other parameters remain at $\Delta S = 540\,\mathrm{mol/m^3}$, $H = 10\,\mathrm{cm}$, $L = 5\,\mathrm{cm}$. (a) $\Delta T = 27\,^\circ\mathrm{C}$, $t = 500\,\mathrm{s}$; (b) $\Delta T = 11\,^\circ\mathrm{C}$, $t = 1000\,\mathrm{s}$.

The K_e reaches another maximum at $t \approx 1770$ s when the flow is composed of three convection layers, as shown in Fig. 4(d). The three-layer structure remains while the convection at the top and the bottom layers reduces gradually, and the convection in the middle becomes more intense; see Fig. 4(e). After that, the flow integrity starts to break down due to the merging of convection layers, leading to a more turbulent status, which can hardly characterize any flow feature. As a result, the K_e remains virtually the same for the rest of the computation.

To consolidate the scenario of the fully developed flow, we conduct another two computations to examine the fully developed flow under different conditions, which are $\Delta T = 11\,^\circ\mathrm{C}$ and $27\,^\circ\mathrm{C}$ corresponding to $\mathrm{Ra}_T = 2.32 \times 10^8$ and 5.70×10^8, respectively. For the case $\Delta T = 27\,^\circ\mathrm{C}$, as indicated by the solid circle of curve A in Fig. 3, the fully developed flow occurs at $t \approx 500$ s, which is composed of three convection layers and the salt-finger vortices have a large aspect ratio of height to width, as shown in Fig. 5(a). The velocity vectors at the transverse plane at $y = D/2$ show that the three convection layers invariably tilt from the hot wall to the cold wall, indicating that the horizontal temperature gradient is so significant that the flow moves robustly from the hot wall towards the cold wall. The flow ends at $t \approx 1450$ s when the multilayer structure breaks down from the top and bottom areas. For the case $\Delta T = 11\,^\circ\mathrm{C}$, as indicated by the solid and open circles of curve C, the flow becomes fully developed at $t \approx 1000$ s and ends $t \approx 1500$ s . The fully developed flow comprises seven convection layers at the most rigorous stage, as shown in Fig. 5(b). However, due to the smaller ΔT applied, the layer thickness is thinner, and the flow is relatively tender.

B. Layer thickness under different boundary conditions

To study the second feature of the fully developed flow, we conduct a wide-range parametric study by focusing on four parameters: $\Delta T = 10\,^\circ\mathrm{C}$, $\Delta S = 540\,\mathrm{mol/m^3}$, $H = 10\,\mathrm{cm}$, $L = 5\,\mathrm{cm}$. For each case studied, one parameter will change while the others remain the same. For example, when we consider the effect of ΔT, the ΔT changes from $8\,^\circ\mathrm{C}$ to $30\,^\circ\mathrm{C}$ by increasing $1\,^\circ\mathrm{C}$ to advance a case [or $\Delta T = 8\,(1)\,30\,^\circ\mathrm{C}$] while the other parameters remain the same. Consequently, there are 23 cases computed. When we study the effect of ΔS, $\Delta S = 5\,(50)\,1150\,\mathrm{mol/m^3}$ is considered so that there are 23 cases computed. When the effect of H is studied, we have $H = 4\,(1)\,20\,\mathrm{cm}$, and there are 17 cases computed. When the effect of L is examined, we have $L = 1\,(1)\,15\,\mathrm{cm}$, and there are 15 cases computed. Consequently, there are a total of 78 cases computed. Note that the $\Delta S = 540\,\mathrm{mol/m^3}$ is equivalent to that the solute is 2 wt % at the top and 5 wt % at the bottom, and so on.

The first case investigated is the effect of ΔT. It is seen from the first row of Fig. 6 that a higher ΔT leads to a larger layer thickness, which is because, for a flow generated with a higher ΔT, the salt fingers are thriving more rigorously and contain higher kinetic energy. As a result, it is
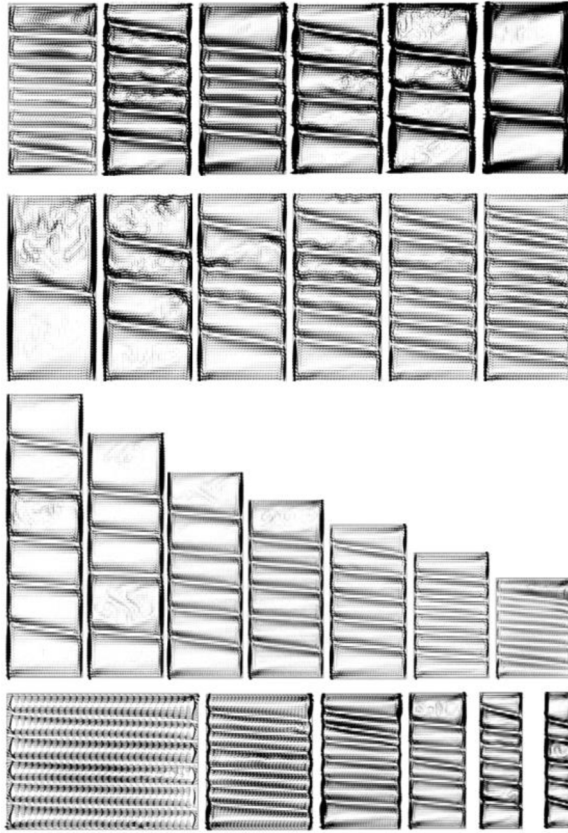
FIG. 6. The convection layers on the transverse plane at $y = D/2$ under different boundary conditions. The first row illustrates the effect of varying ΔT, from left to right: $\Delta T = 11, 15, 18, 20, 24, 27\,°C$. The second row illustrates the effect of varying ΔS, from left to right: $\Delta S = 155, 205, 255, 305, 355, 405\,mol/m^3$. The third row illustrates the effect of varying H, from left to right: $H = 18, 16, 14, 12, 10, 8, 6$ cm. The fourth row illustrates the effect of L, from left to right: $L = 14, 8, 6, 4, 3, 2$ cm.

necessary to have a thicker convection layer to accommodate these robustly active salt fingers. To confirm this scenario, we define a layer thickness $h_C = H/n$ in which n is the number of convection layers. By comparing the h_C and the theoretical counterpart h_T of (1), we obtain that $h_C \approx 0.9h_T$ for $\Delta T = 11\,°C$ and $h_C \approx 0.78h_T$ for $\Delta T = 24\,°C$, which are in good agreement with the measurements of Chen *et al.* [2].

For the effect of ΔS, the results shown in the second row of Fig. 6 illustrate that the n increases monotonically with increasing ΔS. More specifically, we have $n = 2$ for $\Delta S = 155\,mol/m^3$, 4 for $205\,mol/m^3$, 5 for $255\,mol/m^3$, 6 for $305\,mol/m^3$, 7 for $355\,mol/m^3$, and 8 for $405\,mol/m^3$. As a result, the h_C decreases from $0.89h_T$ to $0.65h_T$ as ΔS increases from 155 to $405\,mol/m^3$, which is also in agreement with (1) that h_T decreases with a larger ΔS.

For the effect of H, the results at the third row of Fig. 6 illustrate that, when H varies from 18 to 6 cm, the n remains at 6 while the h_C decreases to accommodate the reduction of H. For the effect of L, for all the cases considered, the n also remains at 6, no matter how small the L is, as shown by the fourth row of Fig. 6. This is because, when the fluid rises along the heated wall, it does not see the cold wall when the box width is sufficiently large. We note that, since we keep ΔS constant when the effect of H is considered, it accordingly leads to that a changing L is having a similar impact to a changing H.
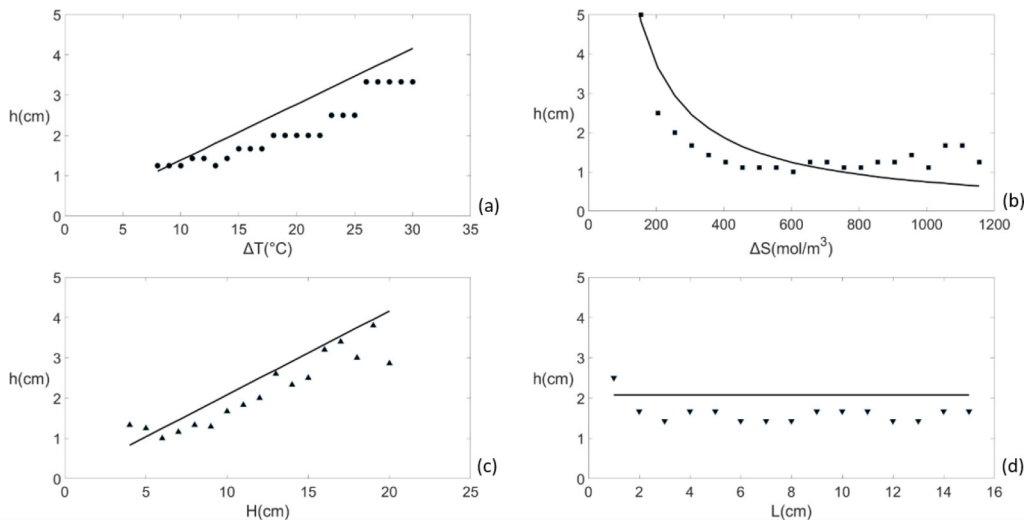
FIG. 7. The layer thickness h_T calculated from (1) accounted for by the straight line or the smooth curve and those measured from the computational results under different boundary conditions. (a) $h_{\Delta T}$ for varying ΔT. (b) $h_{\Delta S}$ for varying ΔS. (c) h_H for varying H. (d) h_L for varying L.

The flow patterns of Fig. 6 demonstrate that the layer thickness changes under different boundary conditions, which raises a question about whether the scaling of the present computation may apply well to the reduced-scale flows in the laboratory and the large-scale flows in oceans. To answer the question, we first consider the flow around the iceberg in Arctic oceans investigated by Huppert and Turner [17] who concluded that the freshwater from the melting iceberg is mainly contained in the horizontal convection layers generated by the interaction between the horizontal temperature gradient and the vertical salinity gradient. To quantify the characteristics of these convection layers, Huppert and Turner [3] conducted a series of experiments in the laboratory with Ra_T ranging $O(10^5)$–$O(10^7)$, which is much larger than the critical $\text{Ra}_T = 15\,000 \pm 2500$ determined by Chen *et al.* [2] while it is close to the iceberg under oceanographic conditions. They proposed that the layer thickness measured in the laboratory follows the relation $h = 0.65h_T$, which is generally smaller than $h = (0.81 \pm 0.10)h_T$ resulting from the experiments for $1.4 \times 10^4 \leqslant \text{Ra}_T \leqslant 5.4 \times 10^4$ [2]. The above experimental results imply that the layer thickness h is smaller than the theoretical prediction h_T when Ra_T is larger, which is comply with the present computational results as explained in the following.

For the 78 cases considered, we calculate the layer thickness by dividing the height of the box, $H = 10$ cm, by the number of layers at the beginning of the fully developed flow. The results are shown in Fig. 7 in which the effects of four boundary conditions are demonstrated separately by the four subfigures. In each subfigure, there are two groups of data; one is the result from computation denoted with symbols, the other is the result from the theory of (1) denoted with a straight line or a smooth curve.

The first effect examined is the temperature difference ΔT shown in Fig. 7(a). By comparing the computational and the theoretical results, we conclude that the layer thickness $h_{\Delta T}$ varies in the range $h_{\Delta T} \approx (0.65\text{–}0.94)h_T$ by decreasing with increasing ΔT. According to the definition of (6), the Ra_T corresponding to the range of ΔT of Fig. 7(a) varies from 8.28×10^4 to 6.21×10^5, confirming that $h_{\Delta T}/h_T$ decreases with increasing Ra_T. Specifically, present computation shows that $h_{\Delta T}$ decreases from $0.94h_T$ to $0.65h_T$ when Ra_T varies from 8.28×10^4 to 6.21×10^5, which is consistent with the experiment of Chen *et al.* [2] that $h = (0.81 \pm 0.10)h_T$ when Ra_T lies in $1.4 \times 10^4 \leqslant \text{Ra}_T \leqslant 5.4 \times 10^4$ in the quantitative sense.

The first effect examined is the temperature difference ΔT shown in Fig. 7(a). By comparing the computational and the theoretical results, we conclude that the layer thickness $h_{\Delta T}$ varies in the range $h_{\Delta T} \approx (0.65\text{–}0.94)h_T$, or $h_{\Delta T} \approx 0.78h_T$ in average. According to the definition of (6), the Ra_T varies from 2.32×10^5 to 4.59×10^7 when ΔT increases from $8\,^\circ\mathrm{C}$ to $30\,^\circ\mathrm{C}$. This result shows a good agreement with Huppert and Turner [3] that $h_{\Delta T} = 0.65h_T$ when Ra_T varies in $O(10^5)\text{–}O(10^7)$ as well as Chen *et al.* [2] that $h = (0.81 \pm 0.10)h_T$ when Ra_T lies in $1.4 \times 10^4 \leqslant \mathrm{Ra}_T \leqslant 5.4 \times 10^4$. The agreement above implies that the present computation can simulate the flow in the laboratory as far as the scaling is concerned.

We note that the layer thickness measured in the laboratory is generally of a scale of 1 cm, while that around the iceberg is of a scale of several meters or larger. Huppert and Turner [3] argued that the convection layers generated in the laboratory can simulate those generated by an iceberg in the ocean as long as the laboratory setup is scaled properly. Consequently, since the present computation can properly simulate that in the laboratory, it is reasonable to infer that it can simulate the flow in the ocean as well.

Regarding the effect of ΔS, as shown in Fig. 7(b), the layer thickness remains at $h_{\Delta S} \approx 0.68h_T$ when ΔS varies from 200 to $500\,\mathrm{mol/m^3}$. As ΔS increases further from 500 to $1000\,\mathrm{mol/m^3}$, the layer thickness increases from $h_{\Delta S} \approx 0.75h_T$ to $h_{\Delta S} \approx 1.52h_T$. Theoretically, as shown by (1), the layer thickness h_T decreases when the salinity gradient increases. In the computation, however, the $h_{\Delta S}$ mostly increases with ΔS, which is a result of the enhancement of the mixing between two layers, as shown in the flow patterns of the second row of Fig. 6.

The other two effects stem from the geometry limitation of the computational domain. When the effect of the height H is considered, as shown in Fig. 7(c), the layer thickness changes within the range $h_H \approx (0.8\text{–}0.9)h_T$. While the effect of the width L is considered, as shown in Fig. 7(d), the change of layer thickness lies in the range $h_L \approx (0.7\text{–}0.8)h_T$. In the case of an iceberg melting in the ocean, the layer thickness follows well with the relation $h = 0.65h_T$, beyond the ranges due to the geometry limitations. This implies that in the ocean when there is no geometry limitation applied, the layer thickness is mostly influenced by the vertical salinity gradient and the horizontal temperature difference.

Finally, it is worth mentioning that the scale of the horizontal convection layer in the laboratory is generally of an order of 1 cm [2–5]. The scale increases dramatically to 5–10 m in the ocean [17] and about 1 m in the lake [18]. The larger layer thickness in the ocean and the lake is because the salinity gradient is smaller [3]. This result follows well with the definition of the layer thickness (1) that a smaller salinity gradient dS/dz leads to a larger layer thickness h_T.

C. Control of buoyancy balance on the layer thickness

To examine the third feature, we calculate the Grashof numbers Gr_r and Gr_s of the convection layer at fully developed flow, which are defined as

$$\mathrm{Gr}_r = \frac{g\alpha\,\Delta T\,h_C^3}{\nu^2}\frac{h_C}{L}, \quad \mathrm{Gr}_S = \frac{g\beta\,\Delta S'\,h_C^3}{\nu^2}\frac{h_C}{L}. \tag{8}$$

In the definitions above, ΔT is the temperature difference applied to the heated wall, $\Delta S'$ is the solute difference across the height of a convection layer, which is obtained by dividing the vertical solute difference ΔS by the number of convection layers n; namely, $\Delta S' = \Delta S/n$ [5]. In either experiment or computation, the layer thickness is usually not uniformly equal. We shall accordingly consider the averaged layer thickness $h_C = H/n$ as the characteristic length for the following calculations except as indicated otherwise.

Based on the definitions of (8), we calculate the 78 pairs of $(\mathrm{Gr}_r, \mathrm{Gr}_s)$ of the fully developed flows by using the physical parameters of Table I and the h_C resulting from computations, and the results are shown in Fig. 8 with solid symbols. It is seen that for all the fully developed flows examined,
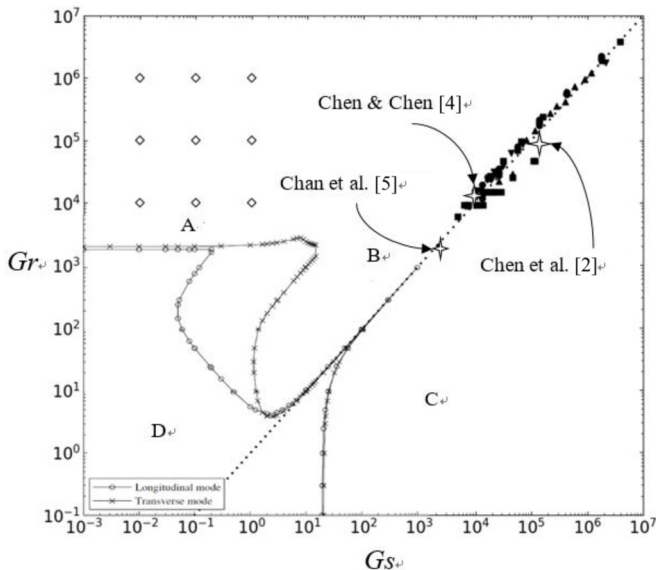
FIG. 8. The stability boundaries of the transverse mode (the curve with crosses) and the longitudinal mode (the curve with open circles) predicted by Chang *et al.* [9] for Le = 100. Letter A denotes the thermal-diffusive regime, B the salt-finger regime, C the solute-diffusive regime, and D the stable regime. The present computation simulates nine thermal-diffusive flows denoted by the nine empty diamonds, and 78 salt-finger flows denoted by the other four solid symbols are the cases considered in Sec. IV B: the solid circle denotes the case of changing ΔT, the solid square denotes changing ΔS, the solid triangle denotes changing H, the upside-down solid triangle denotes changing L. All these 78 symbols scatter in the vicinity of the straight line $\mathrm{Gr}_r = \mathrm{Gr}_s$. The experimental results of Chen *et al.* [2], Chen and Chen [4], and Chan *et al.* [5] are presented in the stability map denoted respectively with an open star.

their corresponding $(\mathrm{Gr}_r, \mathrm{Gr}_s)$ locate invariably in the vicinity of the straight line $\mathrm{Gr}_r = \mathrm{Gr}_s$. After applying the Gr_r and Gr_s of (8), the h_T of (1), and the relation between $\Delta S'$ and ΔS, which is

$$\frac{\Delta S'}{\Delta S} = \frac{h_C}{H}, \tag{9}$$

we obtain

$$\frac{\mathrm{Gr}_S}{\mathrm{Gr}_r} = \frac{h_C}{h_T}. \tag{10}$$

Physically, $\mathrm{Gr}_r = \mathrm{Gr}_s$ means, in the convection layer, that the positive thermal buoyancy balances with the negative solute buoyancy, which was the original assumption made by Chen *et al.* [2] to derive the h_T (1). Since, as shown by (10), $\mathrm{Gr}_r = \mathrm{Gr}_s$ leads to $h_C = h_T$, one may accordingly imply that the convection layer determines its thickness to maintain a buoyancy-balance status.

We also found that $\mathrm{Gr}_r = \mathrm{Gr}_s$ of the fully developed flow applies well to previous experiments. To show this finding, we calculate the $(\mathrm{Gr}_r, \mathrm{Gr}_s)$ of three fully developed flows observed experimentally. The first flow was observed in experiment 8 of Chen and Chen [4]; there were eight convection layers in the box of a height of 9.5 cm, as shown in their Fig. 2. By applying the experimental conditions $\Delta T = 10\,^{\circ}\mathrm{C}$ and $\Delta S = 3\%$ and relevant physical parameters of Table I, we obtain $\mathrm{Gr}_r = 1.204 \times 10^4$ and $\mathrm{Gr}_s = 1.083 \times 10^4$. As shown by the blank star in Fig. 8, the $(\mathrm{Gr}_r, \mathrm{Gr}_s)$ locates slightly above the straight line $\mathrm{Gr}_r = \mathrm{Gr}_s$. The second flow was observed by Chan *et al.* [5], who experimented with the same box under $\Delta T = 6\,^{\circ}\mathrm{C}$ and $\Delta S = 3\%$. As shown
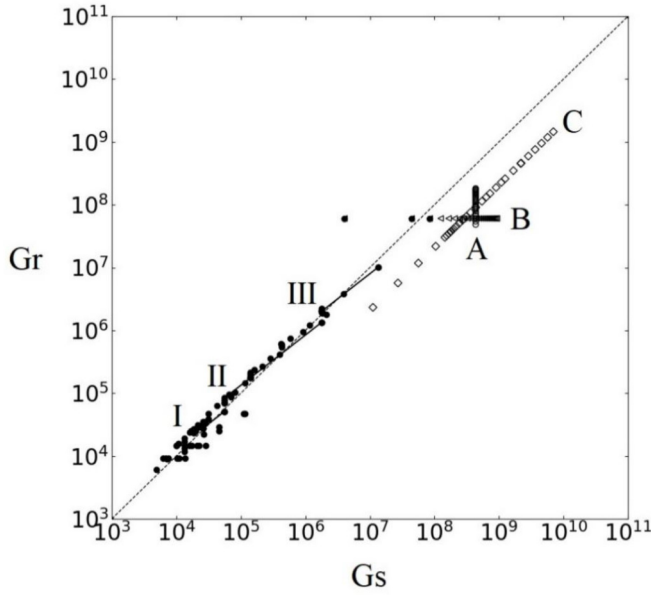
FIG. 9. The $(\mathrm{Gr}_r, \mathrm{Gr}_s)$ of the cases under different boundary conditions. There are two groups of data shown in the figure. The first group is the $(\mathrm{Gr}_r, \mathrm{Gr}_s)$ of the 78 cases considered in Sec. IV, which is shown respectively by line A for $\Delta T = 8(1)30\,^\circ\mathrm{C}$, line B for $\Delta S = 5\ (50)\ 1155\,\mathrm{mol/m}^3$, and line C for $H = 4\ (1)$ 20 cm and $L = 1\ (1)\ 15$ cm. The second group is composed of three tracks of the changing $(\mathrm{Gr}_r, \mathrm{Gr}_s)$ at different ΔT. They are line I for $\Delta T = 11\,^\circ\mathrm{C}$, line II for $\Delta T = 18\,^\circ\mathrm{C}$, and line III for $\Delta T = 27\,^\circ\mathrm{C}$. The flow structures corresponding to line II are shown in Fig. 4. The solid circles are the $(\mathrm{Gr}_r, \mathrm{Gr}_s)$ of the fully developed flows shown in Fig. 8.

in their Fig. 1, the flow was composed of 11 convection layers. After calculating, we obtain $\mathrm{Gr}_r = 2.023 \times 10^3$ and $\mathrm{Gr}_s = 2.204 \times 10^3$, showing again that the $(\mathrm{Gr}_r, \mathrm{Gr}_s)$ locates slightly below the straight line $\mathrm{Gr}_r = \mathrm{Gr}_s$. The third flow was observed by Chen *et al.* [2], who experimented with a larger box having a height of 29.85 cm, a length of 29.85 cm, and a width of 12.7 cm. Under the conditions $\Delta T = 13.6\,^\circ\mathrm{C}$ and $\Delta S = 12\%$, they ended up with a fully developed flow containing 13 convection layers, as shown in their Fig. 4. After calculating, we obtain $\mathrm{Gr}_r = 0.901 \times 10^5$ and $\mathrm{Gr}_s = 1.466 \times 10^5$, showing that the $(\mathrm{Gr}_r, \mathrm{Gr}_s)$ locates slightly below the straight line $\mathrm{Gr}_r = \mathrm{Gr}_s$. These experimental results constantly confirm that the convection layer fully developed is in a buoyancy-balance status.

V. BUOYANCY-BALANCE STATUS DURING TRANSITION

More interestingly, as we will show in this section, the buoyancy-balance status holds for the fully developed flow and the flow during the transition. We elucidate this scenario by showing the change of the $(\mathrm{Gr}_r, \mathrm{Gr}_s)$ of the flows occurring through the unsteady process. The first case considered is for $\Delta T = 18\,^\circ\mathrm{C}$, and the evolution of flow structure has been demonstrated in Fig. 4. The $(\mathrm{Gr}_r, \mathrm{Gr}_s)$ corresponding to each flow of Fig. 4 is calculated, and the results are shown by line II of Fig. 9. Line II shows that, as the convective flow changes dramatically from a six-layer formation at $t = 100$ s [Fig. 4(a)] to a three-layer formation at $t = 2300$ s [Fig. 4(e)], both Gr_r and Gr_s change significantly from about $O(10^4)$ to $O(10^6)$, while the $(\mathrm{Gr}_r, \mathrm{Gr}_s)$ remains in the vicinity of the straight line $\mathrm{Gr}_r = \mathrm{Gr}_s$. This result applies to the other two cases $\Delta T = 11\,^\circ\mathrm{C}$ and $27\,^\circ\mathrm{C}$ investigated in Sec. IV, as shown by lines I and III of Fig. 9, respectively.
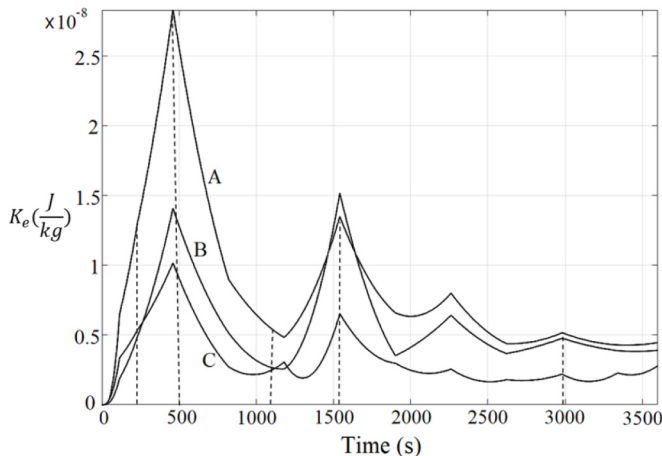
FIG. 10. The time evolutions of the kinetic energy averaged over three longitudinal planes: curve A is for $x = L/5$, curve B for $x = 4L/5$, curve C for $x = L/2$. The case considered corresponds to $\mathrm{Gr}_r = 1 \times 10^5$ and $\mathrm{Gr}_s = 1.0083$.

We stressed in Sec. IV that the reason why the $(\mathrm{Gr}_r, \mathrm{Gr}_s)$ stays in the vicinity of the straight line $\mathrm{Gr}_r = \mathrm{Gr}_s$ is because the convection layer intends to stay in a buoyancy-balance status as it evolves with time. This scenario, however, does not hold before the layer formation begins. To show this, we calculate the $(\mathrm{Gr}_r, \mathrm{Gr}_s)$ of the 78 boundary conditions considered, and the results are shown as lines A, B, and C in Fig. 9. Please note that the boundary condition reflects a status at the beginning of computation when no convection layer has yet formed. It is seen that the $(\mathrm{Gr}_r, \mathrm{Gr}_s)$ distributes widely at the beginning, and most of them are away from $\mathrm{Gr}_r = \mathrm{Gr}_s$. Apparently, the physical configuration before the convection layers form cannot offer an environment in which the buoyancy balance can sustain. However, after the convection layers form, the convection layer adjusts its thickness to keep the buoyancy-balance status valid. We note that, in calculating the $(\mathrm{Gr}_r, \mathrm{Gr}_s)$ for the status before the layer formation, the H is taken as the characteristic length, and the ΔS is used to replace $\Delta S'$.

We have now revealed a clear picture of the convective flow generated by applying a horizontal temperature gradient to destabilize the vertically stable salinity gradient. After the instability is triggered, the quiescent fluid becomes convective. It develops swiftly into a multilayer flow, which is sustained in a buoyancy-balance status until it breaks down through a cascade of the merging between layers. During the flow development, the $(\mathrm{Gr}_r, \mathrm{Gr}_s)$ of the quiescent fluid decreases by several orders of magnitude to that of the multilayer flow. It means that the physical configuration under the boundary condition prescribed is far away from the buoyancy-balance status, which resumes when the layer formation begins and is sustained in due course of the unsteady process by changing the layer thickness. Consequently, the $(\mathrm{Gr}_r, \mathrm{Gr}_s)$ of the convection layer locates invariably in the vicinity of the straight line $\mathrm{Gr}_r = \mathrm{Gr}_s$, and the computed layer thickness h_C is virtually the same as the theoretical counterpart h_T. More precisely, as long as the convection layer forms, it maintains a buoyancy-balance status in which both $\mathrm{Gr}_r \approx \mathrm{Gr}_s$ and $h_C \approx h_T$ hold. Nevertheless, the convective flow may not always develop into the multilayer flow, such as the case belonging to the thermal-diffusion regime, as we shall show in the next section.

VI. FLOW IN THE THERMAL-DIFFUSION REGIME

The quiescent state at the beginning may not develop into a multilayered flow when the boundary conditions are in an extreme situation, such as when the positive thermal buoyancy is much larger than the negative solute buoyancy so that the $(\mathrm{Gr}_r, \mathrm{Gr}_s)$ locates in the thermal-diffusion regime of
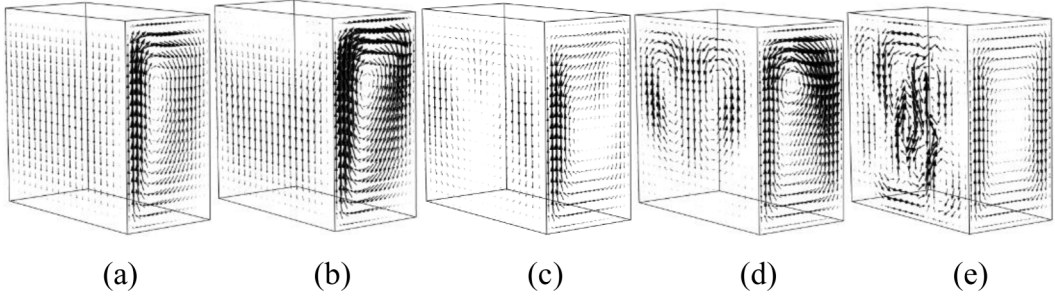
FIG. 11. The convective flow patterns at different times. (a) 200 s, (b) 500 s, (c) 1100 s, (d) 1550 s, (e) 3000 s. The velocity vectors account for the flow on the longitudinal plane at $x = L/2$ and the flow on the transverse plane at $y = D/2$. The velocity vectors in (a)–(d) are of the same amplitude scale, while those in (e) are magnified ten times to demonstrate the flow structure more clearly.

Fig. 8. In such a case, the convective flow development will differ from those investigated in Secs. IV and V. To examine this difference, we conduct a set of computations for nine cases, which are $\Delta T = 0.166, 0.0166, 0.001\,66\,°\mathrm{C}$ corresponding to $\mathrm{Gr}_r = 1 \times 10^6, 1 \times 10^5, 1 \times 10^4$ and $\Delta S = 1.25 \times 10^{-6}, 1.25 \times 10^{-7}, 1.25 \times 10^{-8}\,\mathrm{mol/m^3}$ corresponding to $\mathrm{Gr}_s = 1.0083, 0.100\,83, 0.010\,083$. The $(\mathrm{Gr}_r, \mathrm{Gr}_s)$'s are shown by the open diamonds in Fig. 8, all of them located in the thermal-diffusion regime. For these cases, we have $\mathrm{Gr}_r \gg \mathrm{Gr}_s$ so that the positive thermal buoyancy is much larger than the negative solute buoyancy. According to (1), it implies that $h_T \gg H$, meaning that the heated fluid will rise along the hot wall until it reaches the top wall, which in turn suggests that the computational domain can only accommodate a single convection cell. Namely, the rectangular box may fill up with a single large circulation.

In the nine cases investigated, we choose the case $\Delta T = 0.0166\,°\mathrm{C}$ (or $\mathrm{Gr}_r = 1 \times 10^5$) and $\Delta S = 1.25 \times 10^{-6}\,\mathrm{mol/m^3}$ (or $\mathrm{Gr}_s = 1.0083$) to illustrate the evolution of the thermal-diffusion flow of regime A. We first show in Fig. 10 the time evolution of the K_e over three longitudinal planes locating respectively at $x = L/5, L/2, 4L/5$. Results show that the change of K_e behaves in an organized way, by going up and down with the period becoming shorter as time evolves. On the other hand, the K_e at different planes reaches a maximum virtually at the same time, which is because $h_T \gg H$, so that the entire box is filled up with a large circulation, as shown in Fig. 11.

The velocity vectors shown in Fig. 11 are those of the transverse plane at $y = D/2$ and the longitudinal plane at $x = L/2$. At $t = 200\,\mathrm{s}$, see Fig. 11(a), the fluid close to the left wall rises rapidly until it impinges upon the top wall. It then turns right to move towards the cold wall and descends along the cold wall until it touches the bottom, forming a complete circulation in the rectangular box. At $t = 500\,\mathrm{s}$, the K_e reaches the first maximum, and the velocity vectors show a more rigorous structure, implying that the circulation has a faster flow speed, as shown in Fig. 11(b). At $t = 1100\,\mathrm{s}$, the K_e reduces to a minimum so that the flow slows down due to the fluid viscosity that smears out the flow momentum, as shown in Fig. 11(c). At $t = 1550\,\mathrm{s}$, however, the K_e increases to another maximum, which is because, as shown in Fig. 11(d), the convective flow separates into two convection cells. After that, as shown in Fig. 11(e), the flow becomes turbulent while it slows down due to the viscous dissipation. Note that the velocity vectors of Fig. 11(e) magnify ten times as large as those of the other subfigures to show the flow structure more clearly.

VII. CONCLUSION

We have conducted a series of three-dimensional computations to study the convective flow resulting from the interaction between a horizontal thermal gradient and a vertically stable solute gradient. When the thermal gradient is larger than the critical, a multilayer convective flow is generated. In each layer, an array of salt-finger vortices prevails, moving in the thermal gradient

direction. Within the convection layer, there exist simultaneously the positive thermal buoyancy and the negative solute buoyancy, which are in balance since $\mathrm{Gr}_r \approx \mathrm{Gr}_s$, which in turn leads to $h_C \approx h_T$, implying that the determination of the layer thickness is a direct result of the buoyancy balance as well. This buoyancy-balance status sustains under a wide range of boundary conditions chosen per those considered by previous experimental studies. However, when the boundary conditions are selected for the case $\mathrm{Gr}_r \gg \mathrm{Gr}_s$ the buoyancy-balance status does not hold. As a result, the convective flow fills up the computational domain with a single large circulation, and no salt finger exists. The single-circulation structure satisfies the definition of h_T in (1) because $\alpha \Delta T \gg \beta \Delta S$ leads to $h_T \gg H$. Finally, we note that the present computations are done with dimensional units while the results are presented with nondimensional parameters such as Gr_r and Gr_s for the convenience of both comparison and explanation.

---

[1] S. Thorpe, P. Hutt, and R. Soulsby, The effects of horizontal gradients on thermohaline convection, J. Fluid Mech. **38**, 375 (1969).

[2] C. F. Chen, D. G. Briggs, and R. A. Wirtz, Stability of thermal convection in a salinity gradient due to lateral heating, Int. J. Heat Mass Transfer **14**, 57 (1971).

[3] H. E. Huppert and J. S. Turner, Ice blocks melting into a salinity gradient, J. Fluid Mech. **100**, 367 (1980).

[4] C. F. Chen and F. Chen, Salt-finger convection generated by lateral heating of a solute gradient, J. Fluid Mech. **352**, 161 (1997).

[5] C. L. Chan, W. Y. Chen, and C. F. Chen, Secondary motion in convection layers generated by lateral heating of a solute gradient, J. Fluid Mech. **455**, 1 (2002).

[6] H. E. Huppert, R. C. Kerr, and M. A. Hallworth, Heating or cooling a stable compositional gradient from the side, Int. J. Heat Mass Transfer **27**, 1395 (1984).

[7] O. S. Kerr, Two-dimensional instabilities of steady double-diffusive interleaving, J. Fluid Mech. **242**, 99 (1992).

[8] O. S. Kerr, Three-dimensional instabilities of steady double-diffusive interleaving, J. Fluid Mech. **418**, 297 (2000).

[9] T. Y. Chang, F. Chen, and M. H. Chang, Three-dimensional stability analysis for a salt-finger convecting layer, J. Fluid Mech. **841**, 636 (2018).

[10] R. A. Wirtz and L. H. Liu, Numerical experiments on the onset of layered convection in a narrow slot containing a stably stratified fluid, Int. J. Heat Mass Transfer **18**, 1299 (1975).

[11] J. C. Heinrich, A finite element model for double-diffusive convection, Int. J. Numer. Meth. Eng. **20**, 447 (1984).

[12] J. W. Lee and J. M. Hyun, Double-diffusive convection in a cavity under a vertical solutal gradient and a horizontal temperature gradient, Int. J. Heat Mass Transfer **34**, 2423 (1991).

[13] K. Kamakura and H. Ozoe, Experimental and numerical analyses of double-diffusive natural convection heated and cooled from opposing vertical walls with an initial condition of a vertically linear concentration gradient, Int. J. Heat Mass Transfer **36**, 2125 (1993).

[14] Y. H. Huang, Three-dimensional simulations of the double-diffusive convection in a rectangular box heating from one side and cooling from the other, Master thesis, National Taiwan University, Taipei, Taiwan (2019), Chap. 2.

[15] J. Tanny and A. B. Tsinober, The dynamics and structure of double-diffusive layers in sidewall-heating experiments, J. Fluid Mech. **196**, 135 (1998).

[16] O. S. Kerr, The criteria for the onset of double-diffusive instabilities at a vertical boundary, Phys. Fluids **12**, 3289 (2000).

[17] H. E. Huppert and J. S. Turner, On melting icebergs, Nature (London) **271**, 46 (1978).

[18] M. Toffolon, A. Wuest, and T. Sommer, Minimal model for double diffusion and its application to Kivu Nyos and Powell Lake, J. Geophys. Res.: Ocean **120**, 6202 (2015).